Vibration Reduction in Rotor Blades Using Active Composite Box Beam

Aditi Chattopadhyay,* Qiang Liu,† and Haozhong Gu‡
Arizona State University, Tempe, Arizona 85287-6106

The vibratory load reduction at a rotor hub using smart materials and closed-loop control is investigated. The principal load-carrying member in the blade is represented by a composite box beam, of arbitrary thickness, with surface bonded self-sensing actuators. A comprehensive theory is used to model the smart box beam. The theory, which is based on a refined displacement field, is a three-dimensional model that approximates the elasticity solution so that the beam cross-sectional properties are not reduced to one-dimensional beam parameters. Both in-plane and out-of-plane warpings are included automatically in the formulation. Next, an integrated rotor vibratory load analysis procedure is developed by coupling an unsteady aerodynamic model with the rotor blade dynamic model based on the smart composite box beam theory. The dynamic deformations of the blade in all three directions, flap, lead lag, and torsion, are included in the analysis. The finite-state, induced-flow model is used for predicting the dynamic loads. The procedure results in significant reductions in the amplitudes of rotor dynamic loads with closed-loop control. Detailed parametric studies are presented to assess the influence of number of actuators and their locations in vibratory hub load reduction.

Nomenclature

A	= piezoelectric layer surface area
a	= blade airfoil lift-curve slope
b	= number of blades
C	= structural damping matrix
C_g	= gyroscopic damping matrix
C_p	= piezoelectric damping matrix
C_T	= rotor thrust coefficient
c	= blade chord
D_c	= centrifugal stiffening coefficient matrix
D_g	= gyroscopic coupling coefficient matrix
d	= piezoelectric coupling coefficient matrix
d_0	= constant component in piezoelectric coupling coefficient matrix
d_1	= linear component in piezoelectric coupling coefficient matrix
E	= applied electric field
E_1, E_2	= Young's moduli in principal directions
F	= aerodynamic force vector
F_i	= ith blade sectional lift
F_x, F_y, F_z	= rotor hub shear forces
f_c	= centrifugal force vector
G	= gain matrix
G_{23}, G_{23}, G_{23}	= shear moduli
h_B	= distance from the midplane to box beam inner surface
h_T	= distance from the midplane to box beam outer surface
i	= electric current vector
K	= structural stiffness matrix
K_s	= additional stiffness matrix due to centrifugal stiffening
$[L_c], [L_s]$	= matrices of harmonic couplings
M	= mass matrix
$[M_c], [M_s]$	= apparent mass matrices
M_x, M_y, M_z	= rotor hub moments
$\bar{Q}$	= elastic stiffness matrix
q	= electric charge vector
R	= rotor radius
r	= blade radial station
r_0	= distance from center point of rotation to the measured point
t	= time
$\bar{t}$	= nondimensional time, Ωt
u	= displacement vector
u_0	= global displacement vector
u_1, u_2	= in-plane displacements
u_3	= out-of-plane displacement
u_{10}, u_{20}	= midplane values of in-plane displacement
u_{30}	= midplane value of out-of-plane displacement
w	= normalized induced velocity at rotor disk
y	= normalized blade lead-lag displacement
z	= normalized blade flap displacement
α, β	= states of induced flow
α_d	= shaft angle of attack
$\delta K, \delta U, \delta W$	= variations in kinetic, strain, and potential energies
ε	= strain vector
$\varepsilon_k, \varepsilon_{k+1}$	= strain defined at the top and bottom surfaces of piezoelectric layer
	= (kth layer)
θ_c, θ_s	= blade cyclic pitches
θ_e	= blade elastic torsion
θ_t	= blade linear twist
θ_0	= blade collective pitch
Λ	= induced strain vector
λ_1	= normalized freestream flow normal to disk
μ	= advance ratio
ρ	= mass density
ρ_a	= air mass density
ρ_s	= blade mass density
σ	= rotor solidity
σ_0	= initial stress vector
$\{\tau_j^{0c}\}, \{\tau_j^{mc}\}, \{\tau_j^{ms}\}$	= induced flow forcing functions
$\phi_j^m(\bar{r})$	= shape function of induced flow
$\phi_\chi, \phi_\eta, \varphi_\chi, \varphi_\eta$	= higher-order terms in displacement field
χ, η, ζ	= Cartesian coordinates
ψ	= blade azimuth angle
ψ_i	= ith blade azimuth angle
ψ_χ, ψ_η	= rotations of the normals to midplane

Ω	= rotor angular velocity
Ω_r	= angular velocity vector
ω	= blade natural frequency
ω_r	= rotation vector
$(\dot{\ })$	= d( )/dt
$(\overset{*}{\ })$	= d( )/d$\bar{t}$

Introduction

IT is well known that vibration reduction is a key issue in rotary wing aircraft design. Recent research has shown that improvements in helicopter vibration reduction can be achieved through the implementation of active control technology by using smart materials.[1−6] Smart composite structures have received considerable attention due to the potential for designing adaptive structures that are both light in weight and possess adaptive control capabilities. Because of the high strength-to-weight ratio offered by composites, structural weight is much less of an issue than it is for isotropic materials. Therefore, it is no longer necessary to use thin-walled sections to model the load-carrying sections of aircraft structures.[7] For example, thick composite spars are currently being used to model the principal load-carrying element in advanced technology blades[8] used in XV-15 tilt rotor aircraft. The classical theories, based on the Kirchoff–Love hypothesis, are no longer adequate for modeling such sections. Also, the incorporation of smart materials into the primary structure introduces additional discontinuities that require careful modeling. Thus, it is essential to develop a general framework for the analysis of rotor blades built around composite sections of arbitrary wall thickness with surface bonded actuators and sensors.

Beam theories associated with isotropic materials have been well understood for years.[9] Recently several composite beam theories have been reported.[10−14] The variational asymptotic approach was used to model beams of arbitrary cross sections[10] and includes in-plane and out-of-plane warping effects. In this approach, the three-dimensional properties of the beam were reduced to one-dimensional beam properties (extension, twist, and two bending terms), and the beam response was approximated based on a one-dimensional analysis. The more comprehensive anisotropic theories rely on a full three-dimensional finite element solution that can become very computationally intensive.[12,13] In other analysis of closed sections[15,16] as well as in some of the three-dimensional finite element models,[13] the classical laminate theory was used to model the individual elements of each beam. This theory, which neglects transverse shear effects, is only appropriate for thin laminates. However, in case of anisotropic material, the changes in interlamina stiffnesses lead to transverse shear stresses even for so-called thin laminates.[17−19] Recently, a mixed variational approach was used by Jung et al.[11] to develop a structural dynamic model of composite rotor blades of arbitrary cross sections. This model includes transverse shear effects and both in-plane and out-of-plane warping terms. However, once again, the three-dimensional properties of the beam were reduced to one-dimensional beam parameters and one-dimensional analysis was used.

The rotor hub vibratory loads are the principal source of helicopter fuselage vibration. The $Nb\Omega$ (where N is an integer, b is the number of blades, and Ω is the rotor angular velocity) harmonic loads, when filtered through the rotor hub, can lead to several problems including structural fatigue and poor ride quality. Therefore, accurate prediction of these loads is fundamental. Rotor vibratory loads primarily arise from 1/rev variation in velocity due to forward flight and severe changes in induced velocity. Accurate unsteady aerodynamic and dynamic models are necessary to describe the physical behavior of the rotor for the vibration reduction study to be meaningful. Several methods have been developed for modeling rotor unsteady loads. The free wake, the prescribed wake, and the newly developed finite-state, induced-flow model described in Refs. 20–23 are available.

Two strategies have been investigated for reducing rotor dynamic loads. The first is controllable twist blades with embedded piezoceramics.[1,2] The second is trailing-edge flaps actuated with piezobimorphs.[4−6] A new type of actuator known as C-block actuator was used by Chattopadhyay et al. to control trailing edge flap deflection.[24] A wind-tunnel experiment was conducted for the
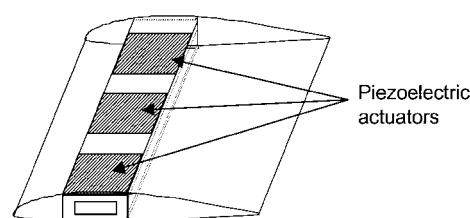

Fig. 1   Rotary wing blade section with piezoelectric actuators.

C-block driven flap to create pitch change of the entire rotor blade section by Clement et al.[25] However, in most of the work, steady or quasi-steady aerodynamic models were used to predict rotor loads. Milgram and Chopra[3] and Koratkar and Chopra[4] used the Leishman–Hariharan aerodynamic model in vibration reduction using an active controlled trailing-edge flap. This theory was developed to model the unsteady aerodynamics of a flapped airfoil in subsonic, compressible flow. Comparison of the Leishman–Hariharan aerodynamic model with classical Theodorsen theory shows that the classical Theodorsen theory is inadequate in the prediction of unsteady airloads in a high-Mach-number aerodynamic environment.[4] A free wake analysis was used in the calculation of dynamic hub loads in Ref. 3, and significant reductions in 4Ω hub loads were reported. Myrtle and Friedmann developed a two-dimensional unsteady compressible aerodynamic model for the dynamic analysis of rotor blades with the combination of blade and actively controlled flap.[5] The effects of compressibility and time-varying flow velocity were included in this work. A comparison of rotor hub load reductions, based on the unsteady aerodynamic model and quasi-steady aerodynamic model, was presented to assess the unsteady effects associated with time-varying free-stream.

The objectives of the present work are twofold. First, a comprehensive analysis technique is developed for the analysis of rotor dynamic loads using a composite rotor blade built around an active box beam. Second, the model is used to investigate reductions in hub dynamic loads using closed-loop control. The principal load-carrying member in the rotor is modeled as a composite box beam of arbitrary wall thickness. Self-sensing piezoelectric (PZT) actuators are surface bonded to the top and bottom surfaces of the horizontal walls of the box beam (Fig. 1). A higher-order, theory-based approach is used to model the smart composite box beam.[26] The theory approximates the elasticity solution so that the beam cross-sectional properties are not reduced to one-dimensional beam parameters. Because the relationships between the induced strain due to actuation and the applied electric field, under moderately high voltage, are nonlinear in nature, formulations presented in the current paper include these nonlinear induced strain effects. An integrated rotor vibratory loads analysis procedure is developed by coupling an unsteady aerodynamic model with the rotor blade dynamic model. The dynamic deformations of the blade in all three directions, flap, lead lag, and torsion, are included in the analysis. Blade dynamic responses are solved in the modal domain. The finite-state, induced-flow model[21] is used for predicting the aerodynamic loads. The 4Ω dynamic forces and moments at the rotor hub are calculated in forward flight using a nonrotating airframe system. Detailed parametric studies are presented to assess the influence of number of actuators and their locations for vibratory load reduction at the rotor hub.

Smart Rotor Blade Model

The principal load-carrying member in the rotor blade is modeled using a composite box beam of arbitrary wall thickness. PZT actuators are surface bonded to the upper and bottom surfaces of the box beam walls. The box beam is modeled by using composite laminates representing the four walls (Fig. 2). A general, higher-order displacement field is developed to model the individual walls, of arbitrary thickness, in the presence of eccentricity (Fig. 2). Details of this theory can be found in Ref. 26. A brief description of the model is presented here for completeness.

The general displacement field, for each plate (Fig. 2), is defined as follows, using the box beam midplane as the reference:
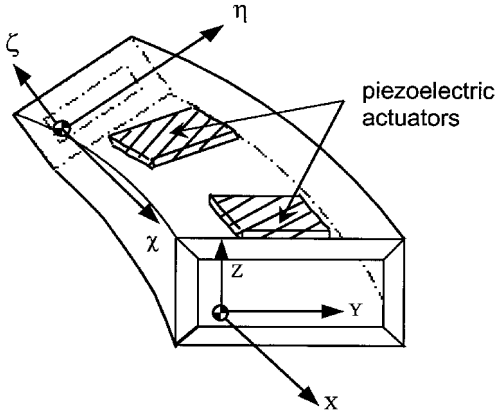
Fig. 2 Modeling composite plate with eccentricity.

$$u_1(\chi, \eta, \zeta) = u_{10}(\chi, \eta) - \zeta\frac{\partial u_3(\chi, \eta)}{\partial \chi} + \zeta\psi_\chi(\chi, \eta)$$

$$+ \zeta^2\phi_\chi(\chi, \eta) + \zeta^3\varphi_\chi(\chi, \eta)$$

$$u_2(\chi, \eta, \zeta) = u_{20}(\chi, \eta) - \zeta\frac{\partial u_3(\chi, \eta)}{\partial \eta} + \zeta\psi_\eta(\chi, \eta)$$

$$+ \zeta^2\phi_\eta(\chi, \eta) + \zeta^3\varphi_\eta(\chi, \eta)$$

$$u_3(\chi, \eta, \zeta) = u_{30}(\chi, \eta) \tag{1}$$

where u_1, u_2, and u_3 are the in-plane and out-of-plane displacements at a point (χ, η, ζ) and u_{10}, u_{20}, and u_{30} represent the displacements at the midplane; the higher-order functions are determined based on the conditions that the transverse shear stresses vanish on the inner and outer surfaces (Fig. 2) of the beam. The following refined displacement field is obtained after satisfaction of the boundary conditions:

$$u_1(\chi, \eta, \zeta) = u_{10}(\chi, \eta) + \zeta\left(\psi_\chi(\chi, \eta) - \frac{\partial u_{30}(\chi, \eta)}{\partial \chi}\right)$$

$$- \frac{\zeta^2}{2}\frac{h_T + h_B}{h_T h_B}\psi_\chi(\chi, \eta) + \frac{\zeta^3}{3h_T h_B}\psi_\chi(\chi, \eta)$$

$$u_2(\chi, \eta, \zeta) = u_{20}(\chi, \eta) - \zeta\left(\psi_\eta(\chi, \eta) - \frac{\partial u_{30}(\chi, \eta)}{\partial \eta}\right)$$

$$- \frac{\zeta^2}{2}\frac{h_T + h_B}{h_T h_B}\psi_\eta(\chi, \eta) + \frac{\zeta^3}{3h_T h_B}\psi_\eta(\chi, \eta)$$

$$u_3(\chi, \eta, \zeta) = u_{30}(\chi, \eta) \tag{2}$$

where h_T and h_B are the distances from the center of the box beam to the inner and outer surfaces of the wall, respectively.

The electromechanical coupling between the applied electric field $\boldsymbol{E}$ and the induced strain $\boldsymbol{\Lambda}$ in the PZT material is governed by the coupling coefficient matrix $\boldsymbol{d}$ that represents PZT material properties. Experimental investigation by Crawley and Lazarus[27] has shown that these coefficients depend on the actual strain in the actuator as well. Based on this observation, an analytical, nonlinear, induced strain model was developed by Chattopadhyay et al.[26] With this approach, the induced strain can be expressed as follows:

$$\boldsymbol{\Lambda} \cong (\boldsymbol{d}_0^T + \boldsymbol{d}_1^T\varepsilon)\boldsymbol{E} \tag{3}$$

where coefficients contained in matrices $\boldsymbol{d}_0$ and $\boldsymbol{d}_1$ can be identified using functional relationships of the strain vs electric field obtained from experimental data of an unconstrained PZT actuator.[27]

The PZT sensors can accurately detect the strain rate when they are connected with a current amplifier and proportional feedback is used for structural vibration control. The feedback actuator voltage is defined through the current developed from the electric charge, which is

$$\boldsymbol{E}(t) = \boldsymbol{G}i(t) = \boldsymbol{G}\dot{q}(t) = \boldsymbol{G}\int_A \bar{\boldsymbol{Q}}\boldsymbol{d}\frac{\dot{\varepsilon}_k + \dot{\varepsilon}_{k+1}}{2}\, dA \tag{4}$$

Aerodynamic Analysis

The induced velocity w, normalized with respect to ΩR, can be expressed as follows:

$$w(\bar{r}, \psi, \bar{t}) = \sum_{m=0}^{4}\sum_{j=m+1, m+3, \ldots}^{9}\phi_j^m(\bar{r})\big[\alpha_j^m(\bar{t})\cos(m\psi)$$

$$+ \beta_j^m(\bar{t})\sin(m\psi)\big] \tag{5}$$

where $\phi_j^m(\bar{r})$ is the shape function and $\bar{r}$ is the normalized radius (normalized with respect to blade radius R). The quantities α and β are the states representing the harmonics. Using the finite-state, induced-flow model,[21,22] the shape function $\phi_j^m(\bar{r})$ can be expanded as

$$\phi_j^m(\bar{r}) = \sqrt{(2j+1)H_j^m}$$

$$\times \sum_{l=m, m+2, \ldots}^{j-1}\bar{r}^l\frac{(-1)^{(l-m)/2}(l+j)!!}{(l-m)!!(l+m)!!(j-l-1)!!} \tag{6}$$

where H_j^m is written as follows:

$$H_j^m = \frac{(j+m-1)!!(j-m-1)!!}{(j+m)!!(j-m)!!} \tag{7}$$

The generalized dynamic wake equations can be written in the following form:

$$[\boldsymbol{M}_c]\left\{\begin{matrix}\vdots\\\{\alpha_j^m\}\\\vdots\end{matrix}\right\}^* + [\boldsymbol{V}][\boldsymbol{L}_c]^{-1}\left\{\begin{matrix}\vdots\\\{\alpha_j^m\}\\\vdots\end{matrix}\right\} = \frac{1}{2}\left\{\begin{matrix}\vdots\\\{\tau_j^{mc}\}\\\vdots\end{matrix}\right\}$$

$$m = 0, 1, 2, 3, 4$$

$$[\boldsymbol{M}_s]\left\{\begin{matrix}\vdots\\\{\beta_j^m\}\\\vdots\end{matrix}\right\}^* + [\boldsymbol{V}][\boldsymbol{L}_s]^{-1}\left\{\begin{matrix}\vdots\\\{\beta_j^m\}\\\vdots\end{matrix}\right\} = \frac{1}{2}\left\{\begin{matrix}\vdots\\\{\tau_j^{ms}\}\\\vdots\end{matrix}\right\}$$

$$m = 1, 2, 3, 4 \tag{8}$$

where $[\boldsymbol{V}]$ is a matrix of flow parameters. These functions establish the relationship between the induced states, the shape functions, and the blade sectional lift. These are expressed as follows:

$$\{\tau_j^{0c}\} = \frac{1}{2\pi}\sum_{i=1}^{4}\left[\int_0^1\frac{F_i}{\rho_a\Omega^2 R^3}\phi_j^0\, d\bar{r}\right]$$

$$\{\tau_j^{mc}\} = \frac{1}{\pi}\sum_{i=1}^{4}\left[\int_0^1\frac{F_i}{\rho_a\Omega^2 R^3}\phi_j^m\, d\bar{r}\right]\cos(m\psi_i)$$

$$\{\tau_j^{ms}\} = \frac{1}{\pi}\sum_{i=1}^{4}\left[\int_0^1\frac{F_i}{\rho_a\Omega^2 R^3}\phi_j^m\, d\bar{r}\right]\sin(m\psi_i) \tag{9}$$

In Eqs. (9), F_i is the sectional lift of the ith blade. From the blade element theory for forward flight, this force can be written as

Table 1   Material properties

Material	Property							
	E_1, GPa	E_2, GPa	$\upsilon 12$	G_{12}, G_{13}, GPa	G_{23}, GPa	ρ, Kg/m$^3 \times 10^3$	d_0, m/V $\times 10^{-12}$	d_1, m/V $\times 10^{-12}$
Graphite/epoxy	134.4	10.3	0.33	5	2	1.477	——	——
PZT	63	63	0.33	24.2	24.2	7.6	247	8.38

$$F_i = \frac{1}{2}\rho_a a\Omega^2 R^3 \bar{c}(\bar{r} + \mu\sin(\psi_i) + \overset{*}{y})\left(\theta_i(\bar{r} + \mu\sin(\psi_i) + \overset{*}{y})\right.$$

$$\left. - w - \lambda_1 - \overset{*}{z} - \frac{\partial z}{\partial \bar{r}}\mu\cos(\psi_i) + \frac{\bar{c}}{2}\overset{*}{\theta_i}\right) \qquad (10)$$

where y and z are the blade lead lag and flapping displacements (normalized with respect to blade radius R). The quantity θ_i is the pitch angle of the ith blade, which can be written as follows:

$$\theta_i = \theta_0 + \theta_t\bar{r} + \theta_c\cos(\psi_i) + \theta_s\sin(\psi_i) + \theta_e \qquad (11)$$

In Eq. (11), θ_0 is the collective pitch, θ_t is the linear twist, and θ_c and θ_s represent the lateral cyclic pitch and the longitudinal cyclic pitch, respectively. The quantity θ_e represents the elastic torsion component that includes the control system stiffness and the blade elastic torsional stiffness. In this work, a total of 33 induced states are used to describe the induced inflow.

Finite Element Formulation

The finite element method is used to implement the coupled theory. The kinetic energy for a helicopter blade with rotation can be expressed as follows:

$$\delta K = \int_A \int_z \rho_s\{\delta[\dot{u} + \Omega_r \times (r_0 + u)]\}[\dot{u} + \Omega_r \times (r_0 + u)]\,dz\,dA$$

$$= -\int_A \int_z \rho_s\delta u\{\ddot{u} + 2\Omega_r \times \dot{u} + \Omega_r * [\Omega_r *(r_0 + u)]$$

$$- (r_0 + u)*(\Omega_r *\Omega_r)\}\,dz\,dA \qquad (12)$$

where r_0 denotes the distance from center point of rotation axis to the measured point at original configuration. The second term on the right-hand side of Eq. (12) represents the contribution of gyroscopic coupling effects and the last two terms are due to centrifugal effects. The partial centrifugal contributions that contain no displacement variables can be defined as a centrifugal force as follows:

$$f_c = \int_A \int_z \rho_s[\Omega_r *(\Omega_r *r_0) - r_0 *(\Omega_r *\Omega_r)]\,dz\,dA \qquad (13)$$

This centrifugal force f_c in Eq. (13) causes the initial stresses in the structure, denoted σ_0, that finally constitutes the partial centrifugal stiffening matrix incorporated with the structural rotations ω_r. The finite element equations are derived using the discretized form of Hamilton's principle, which is stated as follows:

$$\delta\Pi = \int_t (\delta K - \delta U - \delta W)\,dt$$

$$= \int_t \left\{ -\int_A \int_z [\rho_s\delta u^T(\ddot{u} + D_g\dot{u} + D_c u) + \delta\varepsilon^T\bar{Q}(\varepsilon - \Lambda)\right.$$

$$\left. + \delta\omega_r^T\sigma_0\omega_r]\,dz\,dA + \int_A \delta u^T q\,dA\right\}\,dt = 0 \qquad (14)$$

The global finite element equations of motion are then expressed as follows:

$$M\ddot{u}_0 + (C + C_g + C_p)\dot{u}_0 + (K + K_s)u_0 = F \qquad (15)$$

where u_0 and F are the nodal displacement vector and aerodynamic force vector [Eq. (10)], respectively. K_s is expressed by the last two terms on the right-hand side of Eq. (12). The PZT damping
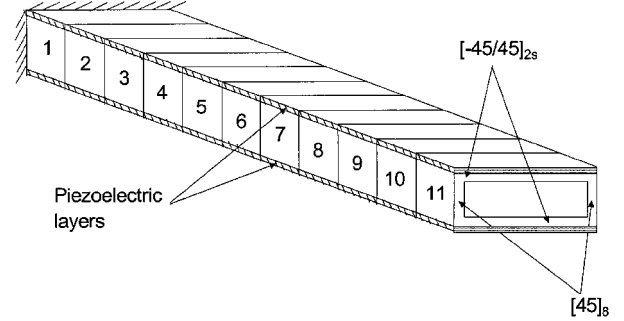
Fig. 3   Composite box beam configuration.

matrix C_p is derived from the PZT induced strain energy expressed in Eq. (14) combined with the feedback control algorithm shown in Eq. (4). Equation (15) is solved using modal analysis that is incorporated using an iterative technique. A total of 11 elements, each with 88 degrees of freedom, resulting in a total of 528 degrees of freedom, are used in the finite element model.

Multiblade coordinates are used to represent the blade equation of motion in the nonrotating system. Seven coupled modes are included in the aeroelastic response analysis. These include three lead-lag modes, three flap modes, and one torsion mode. Combining Eq. (8) with Eq. (15), differential equations for a coupled rotor aeroelastic model are obtained. A fourth-order Runge–Kutta solver is used to obtain numerical results. Once the induced velocity coefficients and the blade displacements are obtained, the rotor vibratory loads are calculated by integrating the aerodynamic, inertial, and centrifugal forces along the blade span.[28]

Results and Discussion

Numerical results are presented using a four-bladed bearingless model rotor with a thrust weighted solidity ratio (C_T/σ) of 0.089. The rotor angular velocity is 28.9 rad/s. The rotor radius is 7.92 m, the dimensionless blade chord is 0.06, and the dimensionless blade root cutout is 0.25. The blade has a rectangular planform and a linear twist of -10 deg. The flow is considered to be inviscid and incompressible.

All results presented in this paper are subject to the same forward flight conditions: $\theta_0 = 15$ deg, $\theta_c = 3.16$ deg, $\theta_s = -1.58$ deg, and $\alpha_d = -3$ deg. Also, $\mu = 0.15$ where μ denotes advance ratio and α_d is the shaft angle of attack. The chordwise center of gravity of blades is located at 25% chord from the leading edge. It coincides with the aerodynamic center and the center of gravity of the box beam. A moderate forward speed is chosen in this work because the effects of compressibility and dynamic stall are not taken into account in the unsteady aerodynamic model. The rotor is trimmed so that there is no first rigid cycle flap in forward flight only. A rigid rotor blade model is used to obtain a rotor trim solution to simplify the problem. This assumption is made due to a lack of flight control equations and wind-tunnel test data in forward flight for this rotor model.

The material properties used for the smart composite beam are listed in Table 1, where E is the Young's modulus and υ is Poisson's ratio. The box beam configuration is as shown in Fig. 3. A stacking sequence of $[-45/45]_{2s}$ is used in the horizontal walls and a stacking sequence of $[45]_8$ is used in the vertical walls. The box beam dimensions are as follows: length $= 7.92$ m, width $= 0.18$ m, and height $= 0.05$ m. The thickness of PZT is 0.196 mm.

A finite element discretized model of the box beam is shown in Fig. 3. For maximum efficiency, the distribution of the actuator

locations must be closely related to the region of high strain rate of the vibration modes. Therefore, for improved first flapping modal damping, the best location for the actuators is element 1 (root area where maximum strain rate occurs). Similarly, elements 1 and 5 represent optimal actuator locations for the control of the second flapping mode and elements 1, 3, 4, 9, and 10 represent the most effective locations for the control of the third flapping mode. Because seven modes are included in the rotor loads analysis, it is difficult to predict the optimal locations of the actuators for the control of all hub loads. Therefore, two different actuator distributions are studied. In the first case (case A), the top and bottom surfaces of the box beam are completely covered by 10 pairs of self-sensing PZT actuators that are surface bonded to the horizontal walls of the box beam (elements 1–10). In the second case (case B), four pairs of discrete, self-sensing PZT actuators are used that are placed on elements 1, 3, 5, and 7. The calculated blade natural frequencies in a vacuum, for the blade built around a smart composite box beam, are presented in Table 2. Some differences are observed in the modal frequencies and mode shapes between the two cases (cases A and B) due to different additional stiffness contributions arising from the different number of actuators used in the two cases.

In Figs. 4a and 4b, the collective fundamental flap response and the collective first torsion modal response are presented for case A

(10 pairs of PZT). The results are compared with and without the application of closed-loop control. From Fig. 4a, it is observed that the convergence of collective flap fundamental response with time is faster due to the effect of closed-loop damping. From Figs. 4b and 4c it is seen that the first collective torsion modal displacement is reduced significantly due to closed-loop control. For example, as shown in Fig. 4c, the collective first torsional displacement decreases by about 30% with control.

The rotor dynamic hub loads are presented in Figs. 5 and 6 for case A. Significant reductions are observed in all forces and moments (F_x, F_y, F_z, M_x, M_y, M_z) in the presence of active control. An increase in damping due to active control obviously lowers the peaks of dynamic rotor hub loads. The magnitudes of the changes are different for different loads. The largest change occurs in 4Ω vertical shear force F_z, which is a critical source of hub vibration (Fig. 5c). The reduction in amplitude of F_z is almost 50%. In general, among all six dynamic rotor hub loads, the pitching moment M_x and the rolling moment M_y contribute most significantly to vehicle vibration. A reduction of about 33% is observed in the amplitude of M_x (Fig. 6a) and a reduction of about 30% is observed in the amplitude of M_y (Fig. 6b).

Figures 7 and 8 present comparisons of the vibratory hub loads for case B (four pairs of PZT). The corresponding reductions in the 4Ω dynamic rotor hub loads are smaller compared to case A, particularly for pitching moment M_y (Fig. 8b) and rolling moment M_x (Fig. 8a). This is expected because in case B, the number of PZT pairs is less than that in case A; therefore, the output power from the actuators in case B is lower than that in case A.

Comparing the results between cases A and B, it is obvious that the reductions in rotor vibratory hub loads strongly depend on the number and location of the actuators. The modal damping due to actuators depends not only on their locations but also on the frequencies
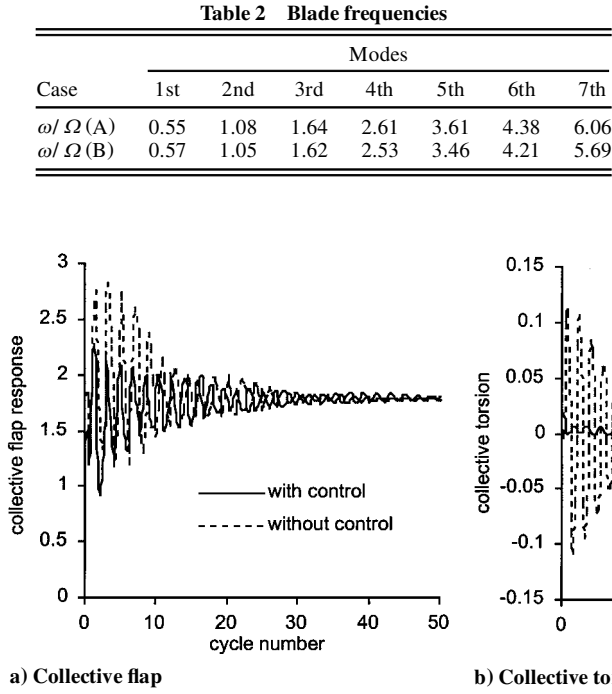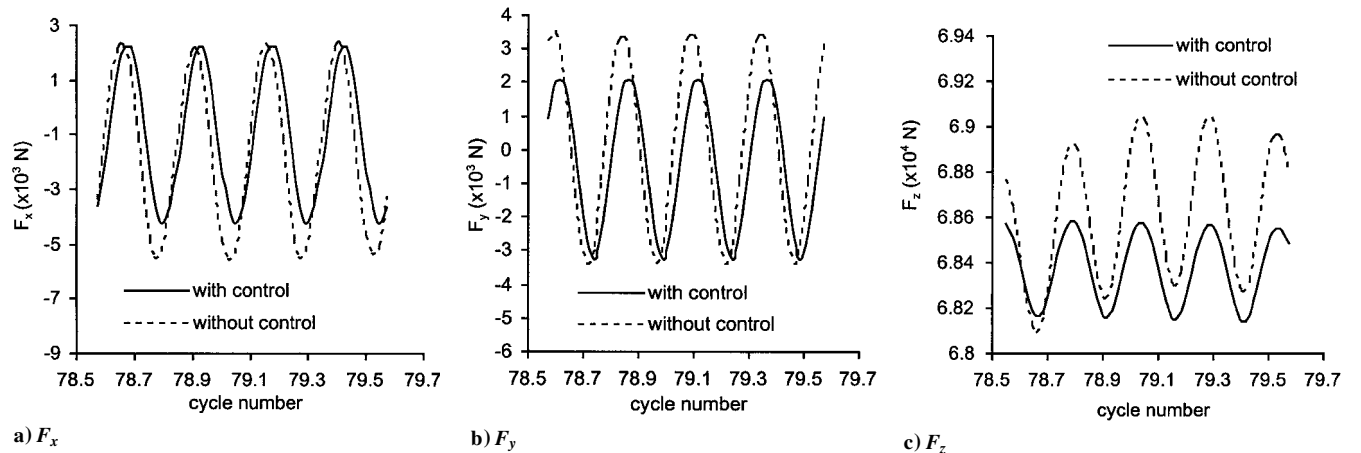
Table 2 Blade frequencies

Case	Modes						
	1st	2nd	3rd	4th	5th	6th	7th
ω/Ω (A)	0.55	1.08	1.64	2.61	3.61	4.38	6.06
ω/Ω (B)	0.57	1.05	1.62	2.53	3.46	4.21	5.69

a) Collective flap   b) Collective torsion   c) Collective torsion

Fig. 4   Rotor response (case A).

a) F_x b) F_y c) F_z

Fig. 5   Rotor hub forces F_x, F_y, and F_z (case A).

a) M_x b) M_y c) M_z

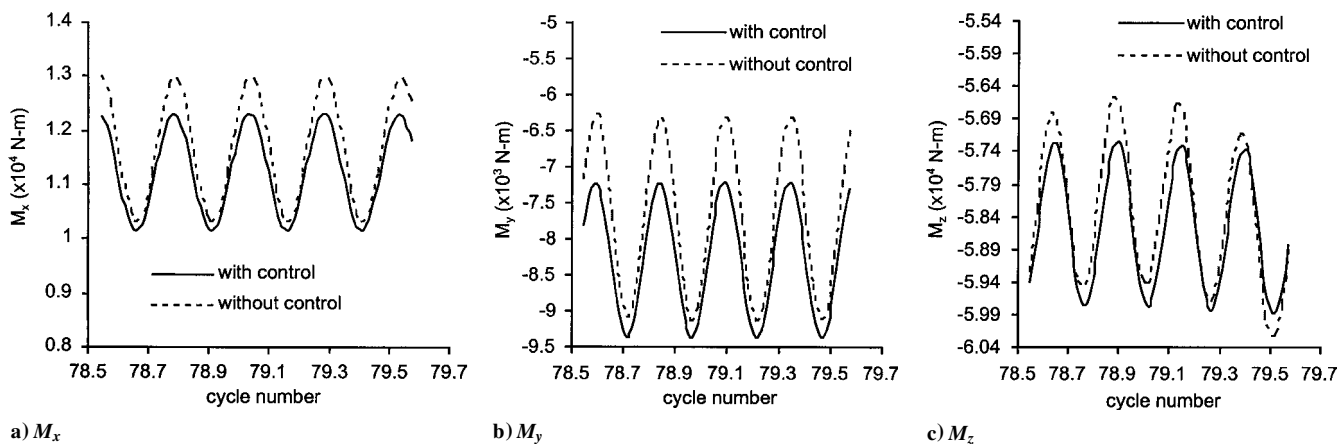Fig. 6 Rotor hub moments M_x, M_y, and M_z (case A).

a) F_x b) F_y c) F_z

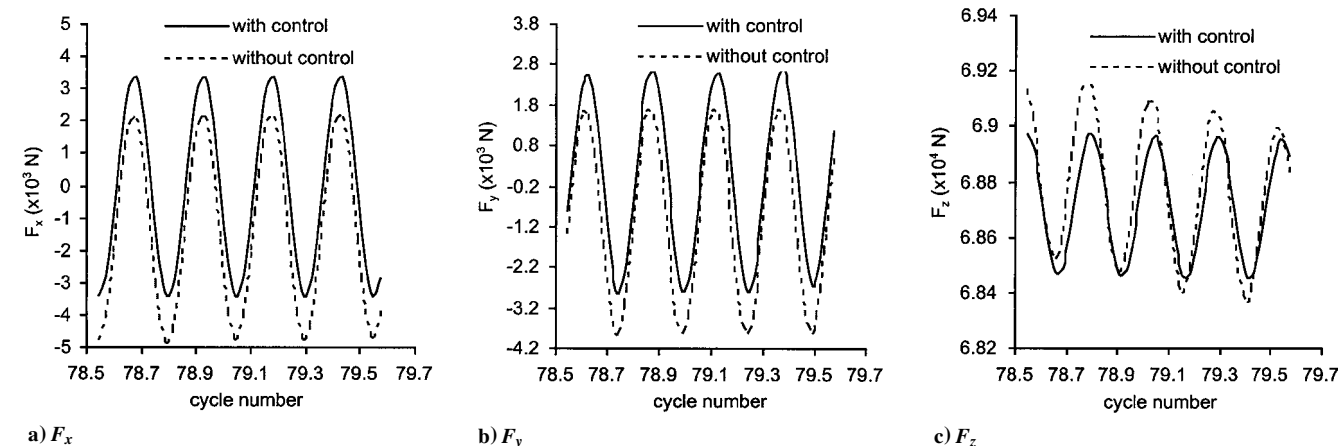Fig. 7 Rotor hub forces F_x, F_y, and F_z (case B).

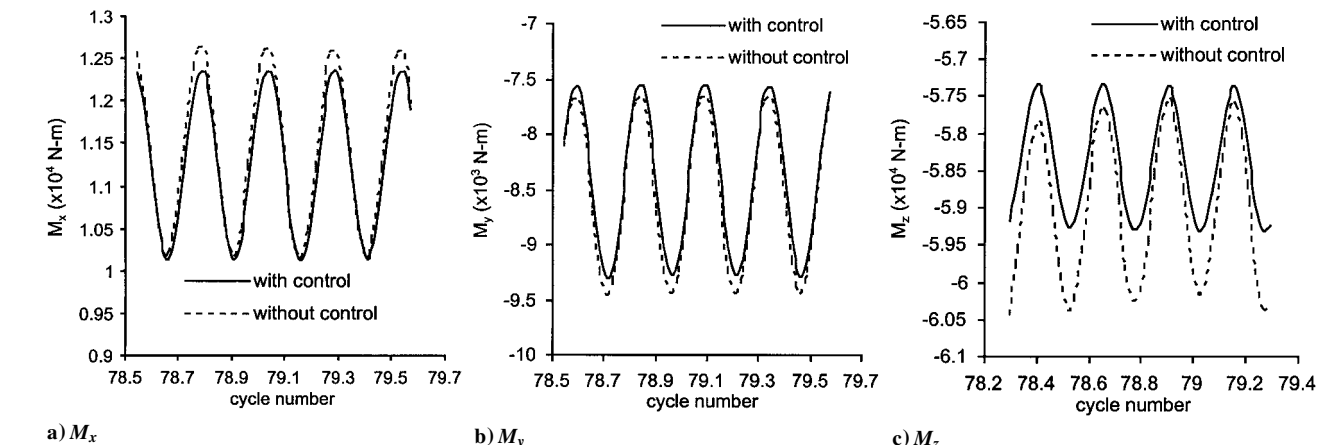a) M_x b) M_y c) M_z

Fig. 8 Rotor hub moments M_x, M_y, and M_z (case B).

at which the system is excited. In case B, where only four pairs of actuators are used, the output power of PZTs is 60% lower than in case A. However, this is not translated linearly to the difference observed in vibration reduction. For example, in case A, about 50% reduction is achieved in F_z, and the corresponding reduction is about 30% in case B, compared to the reference. This indicates the presence of a nonlinear tradeoff between actuator power and active control.

Conclusion

In this paper, reductions in rotor hub dynamic loads are investigated using smart materials and closed-loop control. A composite box beam with surface bonded self-sensing PZT actuators is used to represent the principal load-carrying member in the blade. The

theory is based on a refined higher-order displacement field that accurately captures the transverse shear effects in anisotropic composites. The developed theory is three-dimensional in nature and approximates the elasticity solution so that the beam cross-sectional properties are not reduced to one-dimensional beam parameters. Both in-plane and out-of-plane warpings are included automatically in the formulation. Next, an integrated rotor vibratory hub loads prediction procedure is developed by coupling an unsteady aerodynamic model with the rotor blade dynamic model. The finite-state, induced-flow model is used for predicting the 4Ω rotor hub dynamic loads. Parametric studies are conducted by varying the placement and the total number of actuators along the blade span. Significant reductions are observed in the magnitudes of dynamic hub loads in

all cases. Convergence of the modal response with time is significantly faster with closed-loop control. The magnitude of reduction strongly depends on the number and location of the actuators. As expected, larger reductions are obtained with an increase in the number of actuators. However, a nonlinear tradeoff is observed between power consumption and vibration reduction.

Acknowledgments

References

[1]Chen, P. C., and Chopra, I., "Wind Tunnel Test of a Smart Rotor with Individual Blade Twist Control," *Smart Structure and Materials 1997: Smart Structures and Integrated System*, Vol. 3041, edited by M. E. Regelbrugge, SPIE—The International Society for Optical Engineering, Bellingham, WA, 1997, pp. 217–230.

[2]Barrett, R., Schliesman, M., and Frye, P., "Design, Development and Testing of a Mini Solid State Adaptive Rotorcraft," *Smart Structure and Materials 1997: Smart Structures and Integrated System*, Vol. 3041, edited by M. E. Regelbrugge, SPIE—The International Society for Optical Engineering, Bellingham, WA, 1997, pp. 231–242.

[3]Milgram, J., and Chopra, I., "Helicopter Vibration Reduction with Trailing Edge Flaps," *Proceeding of the 36th AIAA/ASME/ASCE/AHS/ASC Structures, Structural Dynamics, and Materials Conference*, AIAA, Washington, DC, 1995, pp. 601–612.

[4]Koratkar, N. A., and Chopra, I., "Testing and Validation of a Froude Scaled Helicopter Model with Piezo-Bimorph Actuated Trailing Edge Flaps," *Smart Structure and Materials 1997: Smart Structures and Integrated System*, Vol. 3041, edited by M. E. Regelbrugge, SPIE—The International Society for Optical Engineering, Bellingham, WA, 1997, pp. 183–205.

[5]Myrtle, T. F., and Friedmann, P. P., "Unsteady Compressible Aerodynamics of a Flapped Airfoil with Application to Helicopter Vibration Reduction," *Proceedings of the 38th AIAA/ASME/ASCE/AHS/ASC Structures, Structural Dynamics, and Materials Conference*, AIAA, Reston, VA, 1997, pp. 224–240.

[6]Straub, F. K., "A Feasibility Study of Using Smart Materials for Rotor Control," *Proceedings of the American Helicopter Society 49th Annual Forum*, American Helicopter Society, Alexandria, VA, 1993, pp. 1321–1333.

[7]Rand, O., "Theoretical Modeling of Composite Rotating Beams," *Vertica*, Vol. 14, No. 3, 1990, pp. 329–343.

[8]McCarthy, T. R., and Chattopadhyay, A., "A Refined High-Order Composite Box Beam Theory," *Composites*, Vol. 28, Pt. B, 1997, pp. 523–534.

[9]Hodges, D. H., Ormiston, R. A., and Peters, D. A., "On the Nonlinear Deformation Geometry of Euler-Bernoulli Beams," NASA TP-1566, April 1980.

[10]Rehfield, L. W., Atilgan, A. R., and Hodges, D. H., "Nonclassical Behavior of Thin-Walled Composite Beams with Closed Cross Sections," *Journal of the American Helicopter Society*, Vol. 35, May 1990, pp. 42–50.

[11]Jung, S. N., Nagaraj, V. T., and Chopra, I., "A Refined Structural Dynamics Model for Composite Rotor Blades," *A Collection of the 1999 AIAA/ASME/ASCE/AHS/ASC Structures, Structural Dynamics, and Materials Conference*, AIAA, Reston, VA, 1999, pp. 2358–2369.

[12]Kosmatka, J. B., and Friedmann, P. P., "Vibration Analysis of Composite Turbopropellers Using a Nonlinear Beam-Type Finite Element Approach," *AIAA Journal*, Vol. 27, No. 11, 1989, pp. 1606–1614.

[13]Stemple, A. D., and Lee, S. W., "Finite Element Model for Composite Beams with Arbitrary Cross-Sectional Warping," *AIAA Journal*, Vol. 26, No. 12, 1988, pp. 1512–1520.

[14]Bauchau, O. A., "A Beam Theory for Anisotropic Materials," *Journal of Applied Mechanics*, Vol. 52, June 1985, pp. 416–422.

[15]Smith, E. C., and Chopra, I., "Formulation and Evaluation of an Analytical Model for Composite Box-Beams," *Journal of the American Helicopter Society*, Vol. 36, July 1991, pp. 23–35.

[16]Chandra, R., Stemple, A. D., and Chopra, I., "Thin-Walled Composite Beams Under Bending, Torsional and Extensional Loads," *Journal of Aircraft*, Vol. 27, No. 7, 1990, pp. 619–626.

[17]Gu, H., and Chattopadhyay, A., "A New Higher Order Plate Theory in Modeling Delamination Buckling of Composite Laminates," *AIAA Journal*, Vol. 32, No. 8, 1994, pp. 1709–1716.

[18]Reddy, J. N., "A General Non-Linear Third-Order Theory of Plates with Moderate Thickness," *International Journal of Non-Linear Mechanics*, Vol. 25, No. 6, 1990, pp. 677–686.

[19]Reddy, J. N., *Energy and Variational Principles in Applied Mechanics*, Wiley, New York, 1984.

[20]Bousman, W. G., "The Response of Helicopter Rotors to Vibratory Airloads," *Journal of the American Helicopter Society*, Vol. 35, No. 4, 1990, pp. 53–62.

[21]Peters, D. A., and He, Chengjian, "Correlation of Measured Induced Velocity with a Finite-State Wake Model," *Journal of the American Helicopter Society*, Vol. 36, No. 3, 1991, pp. 59–71.

[22]He, C.-J., "Development and Application of a Generalized Dynamic Wake Theory for Lifting Rotors," Ph.D. Dissertation, Dept. of Aerospace Engineering, Georgia Inst. of Technology, Atlanta, GA, July 1989.

[23]Heffernan, R. M., Yamauchi, G. K., Gaubert, M., and Johnson, W., "Hub Loads Analysis of the SA349/2 Helicopter," *Journal of the American Helicopter Society*, Vol. 35, No. 1, 1990, pp. 51–63.

[24]Chattopadhyay, A., Seeley, C. E., and Mitchell, L., "Design of a Smart Flap Using Polymeric C-Block Actuators and a Hybrid Optimization Technique," *Smart Materials and Structures*, Vol. 6, 1997, pp. 134–144.

[25]Clement, J. W., Brei, D., and Barrett, R., "Wind-Tunnel Testing of a High Authority Airspace Insensitive Rotor Blade Flap," *A Collection of the 1999 AIAA/ASME/ASCE/AHS/ASC Structures, Structural Dynamics, and Materials Conference*, AIAA, Reston, VA, 1999, pp. 2414–2424.

[26]Chattopadhyay, A., Gu, H., and Liu, Q., "Modeling of Smart Composite Box Beams with Nonlinear Induced Strain," *Composites*, Vol. 30, Pt. B, 1999, pp. 603–612.

[27]Crawley, E. F., and Lazarus, K. B., "Induced Strain Actuation of Isotropic and Anisotropic Plates," *Proceedings of the 30th AIAA/ASME/ASCE/AHS/ASC Structures, Structural Dynamics, and Materials Conference*, AIAA, Washington, DC, 1989, pp. 2000–2010.

[28]Johnson, W., *Helicopter Theory*, Princeton Univ. Press, Princeton, NJ, 1980, pp. 384–430.

A. Messac
Associate Editor